ACSNANO

www.acsnano.org

ARTICLE

Reactive Oxygen Species Activatable Heterodimeric Prodrug as Tumor-Selective Nanotheranostics

Meijuan Jiang, Jing Mu,* Orit Jacobson, Zhantong Wang, Liangcan He, Fuwu Zhang, Weijing Yang, Qiaoya Lin, Zijian Zhou, Ying Ma, Jing Lin, Junle Qu, Peng Huang,* and Xiaoyuan Chen*

Cite This: https://dx.doi.org/10.1021/acsnano.0c05722

Read Online

ACCESS | Metrics & More | Article Recommendations | Supporting Information

ABSTRACT: Nanotheranostics based on tumor-selective small molecular prodrugs could be more advantageous in clinical translation for cancer treatment, given its defined chemical structure, high drug loading efficiency, controlled drug release, and reduced side effects. To this end, we have designed and synthesized a reactive oxygen species (ROS)-activatable heterodimeric prodrug, namely, HRC, and nanoformulated it for tumor-selective imaging and synergistic chemo- and photodynamic therapy. The prodrug consists of the chemodrug camptothecin (CPT), the photosensitizer 2-(1-hexyloxyethyl)-2-devinyl pyropheophorbide-a (HPPH), and a thioketal linker. Compared to CPT- or HPPH-loaded polymeric nanoparticles (NPs), HRC-loaded NPs possess higher drug loading capacity, better colloidal stability, and less premature drug leakage. Interestingly, HRC NPs were almost nonfluorescent due to the strong $\pi-\pi$ stacking and could be effectively activated by endogenous ROS once entering cells. Thanks to the higher ROS levels in cancer cells than normal cells, HRC NPs could selectively light up the cancer cells and exhibit much more potent cytotoxicity to cancer cells. Moreover, HRC NPs demonstrated highly effective tumor accumulation and synergistic tumor inhibition with reduced side effects on mice.

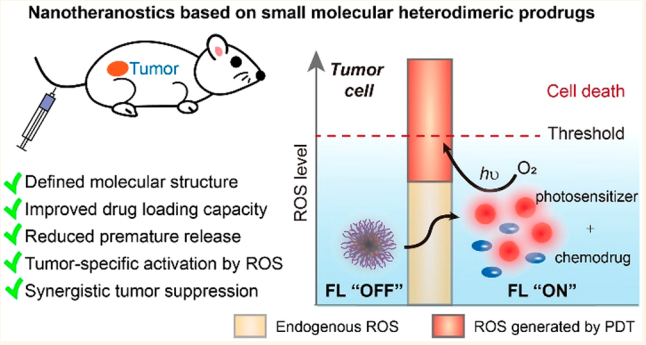

KEYWORDS: *activatable fluorescence imaging, nanotheranostics, reactive oxygen species, prodrug, synergistic therapy*

The past decades have witnessed great progress in cancer treatment, while challenges remain before the goal of precision medicine can be achieved. Though being the main conservative approach for cancer treatment, anticancer drugs often suffer from rapid blood clearance, drug resistance, and severe side effects.[1−3] In order to alleviate the side effects and improve the therapeutic selectivity to cancer cells, the concept of a prodrug, which is usually inert and can be converted to active drug molecules in response to a physiological stimulus, has been proposed.[4,5] By taking advantage of the abnormality of the tumor microenvironment, such as acidity, redox potential, hypoxia, overexpressed enzymes, *etc.*, various types of stimuli-activatable prodrug strategies have been explored.[4,6−12] Among them, reactive oxygen species (ROS) have attracted extensive interest due to their higher levels in tumor areas than normal tissue and critical roles in tumor proliferation and progression.[5,13−18] ROS are key mediators of cell metabolism and functions and usually exist in several forms, including superoxide (O_2^-), hydroxyl radical ($^{\bullet}OH$), singlet oxygen ($^1O_2$), hydrogen peroxide (H_2O_2), and so on. By utilizing ROS-responsive moieties, cancer-targeted prodrugs could be developed for tumor diagnosis, therapy, and theranostics.

The common design of a prodrug is usually to encapsulate the active drugs in an activatable polymeric carrier or conjugate the drugs to the polymer side chain *via* an activatable linker, in order to achieve the optimal pharmacokinetic and pharmacodynamic characteristics. Currently, a variety of macromolecules and polymers have been developed as carriers to deliver drugs to the tumor site.[5,13,19−25] However, most of the developed systems are far from satisfactory and often face the limitations of low drug loading capacity and premature drug release. To solve these problems, further modification of drug carriers is employed, but

Received: July 10, 2020
Accepted: November 13, 2020

Scheme 1. (A) Scheme of prodrug HRC encapsulated by F127 (HRC@F127 nanoparticles), which is activated by reactive oxygen species (ROS), for cancer imaging and synergetic chemo- and photodynamic treatment. (B) Schematic illustration of the mechanism of the selectivity of the prodrug HRC to cancer cells over normal cells.

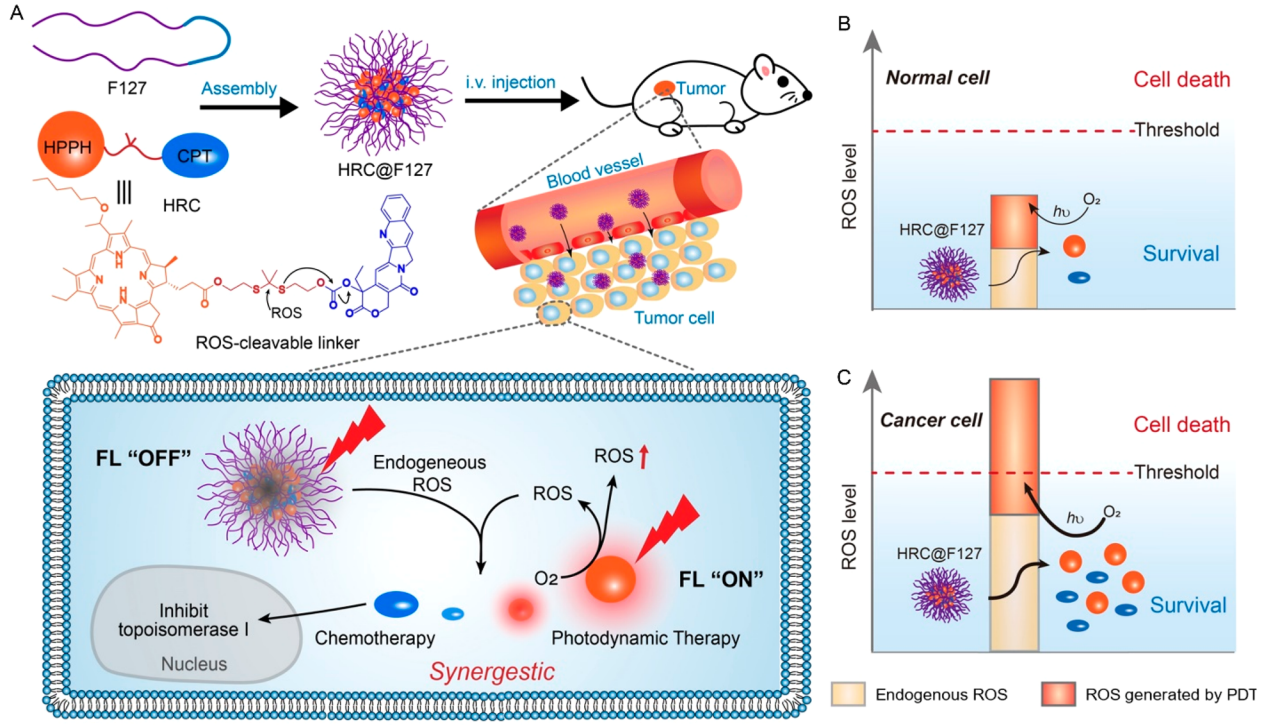

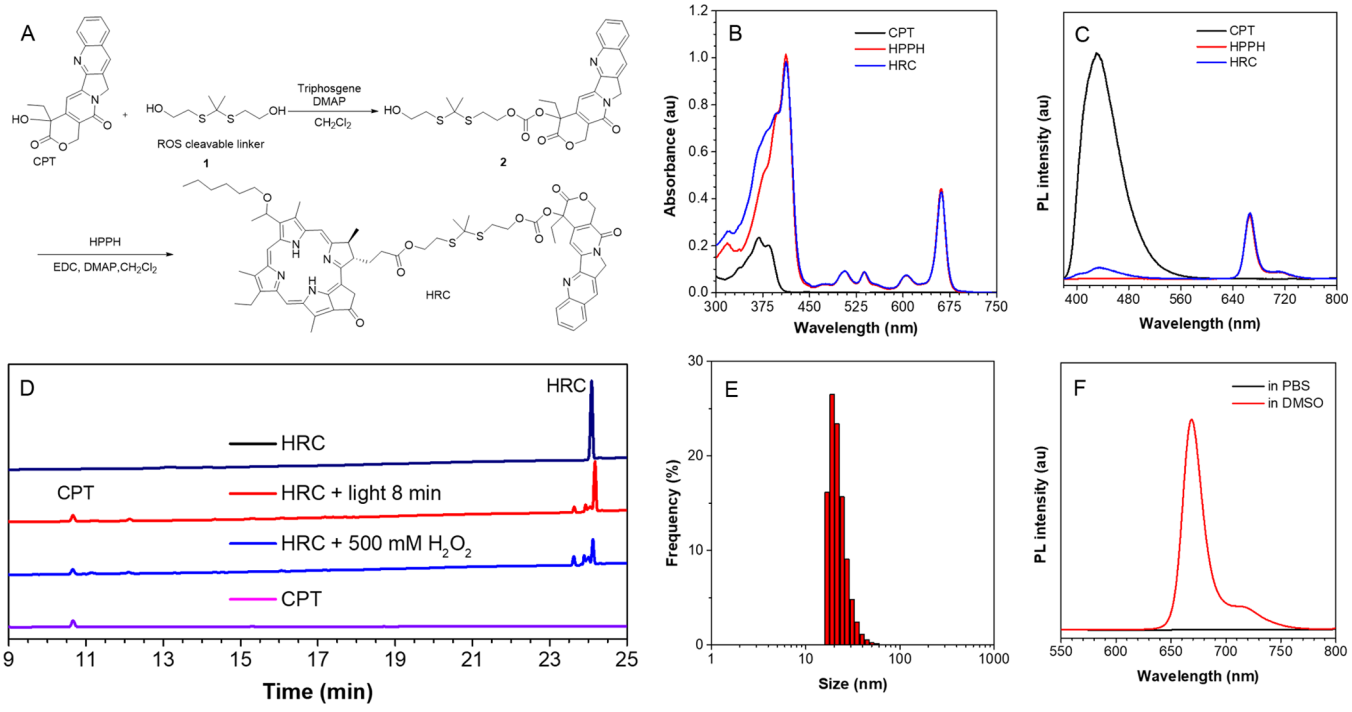

Figure 1. (A) Synthetic route of HRC. (B) UV−vis absorption and (C) photoluminescence (PL) spectra of CPT, HPPH, and HRC in DMSO. Concentration = 10 μM. Ex = 365 nm. (D) HPLC elution spectra of HRC under different conditions: control group, with light irradiation for 8 min or incubation with 500 mM H_2O_2 for 1 h. Laser intensity: 100 mW/cm^2. (E) Size distributions of HRC@F127 analyzed by dynamic laser scattering (DLS). (F) PL spectra of HRC@F127 in PBS and HRC in DMSO. Concentration = 20 μM.

their clinical translation is potentially hindered by their polymeric structural complexity.[26] In contrast, small molecular prodrugs with clear chemical structure are more advantageous in clinical translation, due to its easy manipulation into nano-formulations with high drug loading efficiency and controlled drug release.[27,28]

Herein, as a proof of concept, we developed a heterodimeric prodrug containing the photosensitizer 2-(1-hexyloxyethyl)-2-

https://dx.doi.org/10.1021/acsnano.0c05722
ACS Nano XXXX, XXX, XXX−XXX

devinyl pyropheophorbide-a (HPPH) and camptothecin (CPT), namely, HRC, with a ROS-cleavable thioketal linker and nanoformulated it with a biocompatible polymer (Pluronic F127) for cancer-selective nanotheranostics (Scheme 1A). After nanoformulation, HRC tends to form aggregates in nanoparticles and exhibits aggregation-caused quenching (ACQ) of its fluorescence,[29−31] enabling its "turn-on" fluorescence imaging of a tumor after activation by the endogenous ROS in tumor cells. Since the tumor microenvironment has a higher ROS level than normal cells (as shown in Scheme 1B), HRC could be more selectively cleaved by the higher ROS of cancer cells and exhibit cancer cell-specific fluorescence imaging and therapy. Upon cleavage by ROS, the designed ROS-activatable linker could liberate both free CPT and HPPH molecules from nanoparticles (NPs) and exhibit cytotoxic effect in a synergistic way to cancer cells, given the fact that CPT is not only a topoisomerase I inhibitor but also a hypoxia-inducible factor-1α (HIF-1α) inhibitor.[32] HIF-1α is a key mediator of tumor hypoxia, and its overexpression could increase the cell survival, progression, and tumor metastasis.[33] In the process of PDT, oxygen molecules are effectively converted into ROS to kill cancer cells, during which the simultaneous inhibition of HIF-1α could render cells more vulnerable to low oxygen levels and exhibit a synergistic cytotoxic effect (Figure S1). Fortunately, HPPH could coordinate with radioactive ^{64}Cu,[31,34,35] and thus detailed pharmacokinetics and biodistribution of HRC could be acquired by positron emission tomography (PET) imaging *in vivo* for better understanding the mechanism of action for HRC-based nanotheranostics. As expected, *in vivo* imaging and anticancer therapy results showed that the nanotheranostics based on HRC exhibited effective tumor accumulation and synergistic tumor therapeutic efficacy with reduced side effects on mice as compared to its monomeric drug-loaded NPs, indicating that the strategy of nanoformulation based on ROS-activatable small molecular prodrug allows for safer and more efficient delivery of anticancer drugs and synergistic tumor suppression with reduced side effects.

RESULTS AND DISCUSSION

Synthesis of Heterodimeric Prodrugs and Characterizations. First, the heterodimeric prodrug HRC was synthesized from commercially available CPT and HPPH *via* a two-step reaction route as shown in Figure 1A. Briefly, the thioketal linker **1** was first obtained according to the previous report (Scheme S1)[36] and reacted with CPT to give compound **2**. Next, **2** was reacted with HPPH through esterification reaction to give HRC. The structure of HRC was confirmed by NMR spectra and ESI-MS analysis (Figures S2 and S3). The UV−vis absorption and photoluminescence spectra were studied and displayed the characteristic spectra of both CPT and HPPH (Figure 1B and C). Interestingly, the emission from the CPT moiety is severely quenched by the HPPH moiety after linking together, as CPT emission spectra overlap well with HPPH absorption spectra and Förster resonance energy transfer (FRET) occurs due to the proximity.[37,38] Then, the ROS generation ability of HRC under light irradiation was tested using dichlorodihydrofluorescein (DCFH) as an ROS indicator (Figure S4). The increase of the green fluorescence at around 514 nm clearly indicated the generation of ROS, due to the oxidization of the nonfluorescent DCFH by ROS to form green fluorescent form DCF.[39,40] HPPH and HRC displayed a similar increasing trend in ROS generation upon light irradiation, suggesting that ROS generation ability of the HPPH part of HRC was not harmed by the conjugation of CPT. Similar results were found using 9,10-anthracenediylbis(methylene)dimalonic acid as a singlet oxygen indicator (Figure S5).

As reported, the thioketal linker is ROS-cleavable, and active drugs were released *via* an intramolecular nucleophilic substitution reaction as shown in Figure 1A upon activation by endogenous ROS or ROS generated by a photosensitizer.[20,21,23,24,36,41−55] To confirm that, we treated the HRC with H_2O_2 or light irradiation and then analyzed the fragments with HPLC (Figure 1D). It can be found that after ROS treatment (H_2O_2 or light irradiation), a peak appeared at 10.65 min, which is denoted as the elution time of free CPT, indicating the release of drug CPT. Meanwhile, the peak of HRC at ∼24.1 min decreased obviously, suggesting the effective cleavage of HRC by ROS.

Nanoformulation of HRC. In cancer nanomedicine, nanoformulation is important for improving colloidal stability and stealth effects.[1,2,56] Polymeric micelles, which consist of a hydrophobic core for drug loading and a PEGylated hydrophilic shell, are one of the most important drug carriers.[57] However, micellar formulations are facing problems of low drug loading and premature drug leakage due to the payloads. When CPT was linked with HPPH, the overall molecular weight and hydrophobicity of HRC were enhanced as hydrophobic carbonate and ester groups were formed from the hydrophilic hydroxy group of CPT and the hydrophilic carboxylic acid group of HPPH, respectively. Thus, HRC was expected to address the above obstacles of their corresponding monomers. To confirm these rationales, we first investigated the drug loading of HRC into the FDA-approved biocompatible polymer Pluronic F127. By nanoprecipitation from DMSO to water, the formed nanoparticles HRC@F127 had an average hydrodynamic size of 23 ± 5 nm (Figure 1E) at a feeding ratio of 0.2. The transmission electron microscopy (TEM) image of the NPs revealed the average dimeter of ∼10 nm, likely due to shrinkage during the drying process (Figure S6A). When the feeding ratio was changed to 0.1 or 0.4, nanoparticles could also be formed with a similar size (Figure S6B and C). The control compound with an uncleavable linker, namely, HCC, and HPPH were also loaded into F127, forming HCC@F127 NPs and HPPH@F127 with similar sizes (21 ± 5 and 19 ± 5 nm, respectively, Figure S7A and B). In contrast, the obtained nanoparticle CPT@F127 *via* the same method had a larger hydrodynamic size of >200 nm (Figure S7C), as most of the drug was retained by passing a 220-nm filter, and these nanoparticles were not stable and precipitated in a few hours. The HRC@F127 were stable, and no visible precipitation was observed after a week and no significant size change was found in both water and biological buffer for 24 h (Figure S8). In addition to the favored stability, HRC@F127 also exhibited a much higher loading efficiency of over 95%, compared to both the CPT- and HPPH-loaded NPs (55% and 76%, respectively). These results confirmed that the formation of HRC greatly enhanced the drug loading efficiency and colloidal stability.

It is expected that the increased hydrophobicity of HRC would reduce the drug leakage during circulation. Therefore, we further investigated the drug release of the monomeric and heterodimeric drugs. The typical release plot of CPT@F127 showed that the release was mainly a diffusion-controlled process and initial burst drug release occurred in the first 2 h due to the weakly bound drugs on the surface of the nanoparticles (Figure S9A). Such a burst release is one of the prevalent drawbacks of micellar formulations to be solved. By contrast,

https://dx.doi.org/10.1021/acsnano.0c05722
ACS Nano XXXX, XXX, XXX−XXX

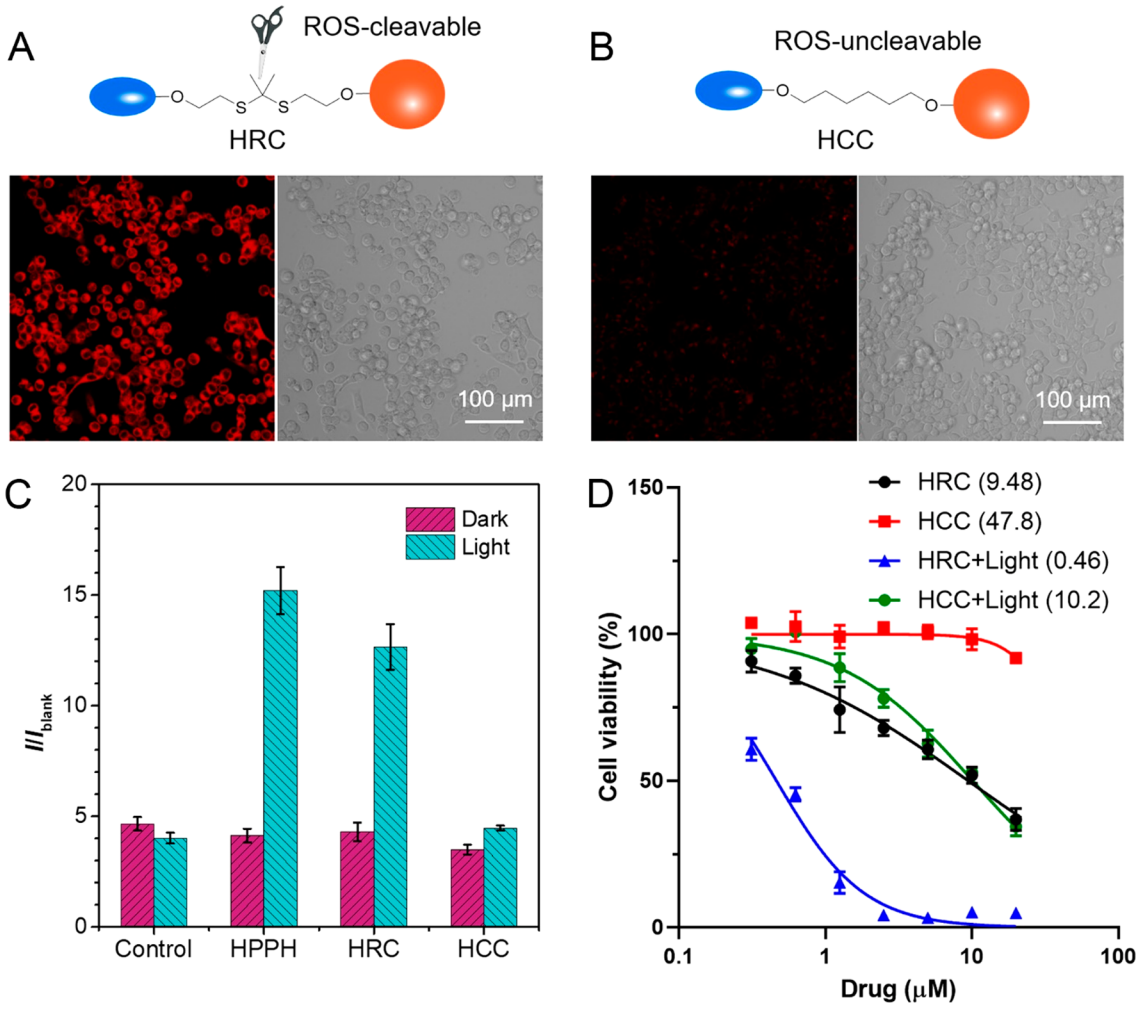

Figure 2. (A, B) Fluorescent and bright field images of HCT116 cells incubated with (A) HRC@F127 and (B) HCC@F127 for 24 h. Concentration = 5 μM. Ex = 561 nm. (C) Relative fluorescence intensity of HCT116 cells incubated with 5 μM HPPH@F127, HRC@F127, and HCC@F127 for 3 h, followed by incubation with 10 μM DCFH-DA for 20 min. Then the cells were treated with/without 671 nm light irradiation (15 mW/cm^2) for 5 min. (D) Cell viability of HCT116 cells evaluated by the MTT assay. Cells were incubated with HRC or HCC for 24 h, followed by treatment with/without 671 nm light irradiation (15 mW/cm^2) for 5 min and incubated for another 24 h.

nearly 98% of HRC remained after 48 h, and it showed a much smaller percentage of leakage (2%) than CPT (75%) and HPPH (24%) (Figure S9B). The results clearly indicated that formation of the heterodimeric prodrug could effectively reduce premature drug release during blood circulation, thus greatly alleviating the side effects.

Intriguingly, the nanoformulation of HRC led to a change of its fluorescence properties. After encapsulation into NPs, the fluorescence of HRC was severely quenched as compared to its DMSO solutions (Figure 1F), suggesting HRC experienced severe ACQ. Such a phenomenon was also found in HPPH@F127 and HCC@F127 (Figure S10). In PBS, HRC was well encapsulated in the hydrophobic core of the polymeric micelles due to its poor water solubility. And in the core, the high concentration of HRC led to the formation of aggregates due to the strong $\pi-\pi$ stacking of the rigid planar HPPH chromophore, consequently quenching the fluorescence.[29,30] In contrast, HRC was well dispersed molecularly and exhibited strong fluorescence in DMSO. Thanks to the ACQ property, HRC@F127 can achieve "turn-on" imaging of cancer cells where HRC@F127 was activated by the high ROS level and release HPPH into the outside environment, and the recovered fluorescence can be utilized for monitoring the drug release of HRC@F127 in cells. To further investigate the activation and drug release of the HRC@F127 NPs, we treated the NPs with H_2O_2 and monitored the particle size changes by dynamic light scattering (DLS) and TEM (Figure S10A–D). Results showed that the particles gradually enlarged over time, suggesting the responsiveness of particles to the oxidative environment.

Selective Cancer Cell Imaging and Therapy. Given the excellent properties of HRC@F127 NPs, we next investigated their intracellular performances on HCT116 human colon cancer cells. To confirm the significance of the ROS-cleavable thioketal linker, a control compound with an uncleavable linker, HCC, was also synthesized and examined. First, HCT116 cells were incubated with HRC@F127 or HCC@F127 for 24 h, and fluorescence images were captured. As shown in Figure 2A and B, cells treated with HRC@F127 showed a high fluorescence intensity, while the control experiments of HCC@F127 showed negligible fluorescence, suggesting that the higher fluorescence in HCT116 was mainly from the released HPPH segments by ROS cleavage. Furthermore, we found that the released HPPH from HRC@F127 could generate much more ROS in cells upon light irradiation as compared to that of HCC, indicated by the

https://dx.doi.org/10.1021/acsnano.0c05722
ACS Nano XXXX, XXX, XXX−XXX

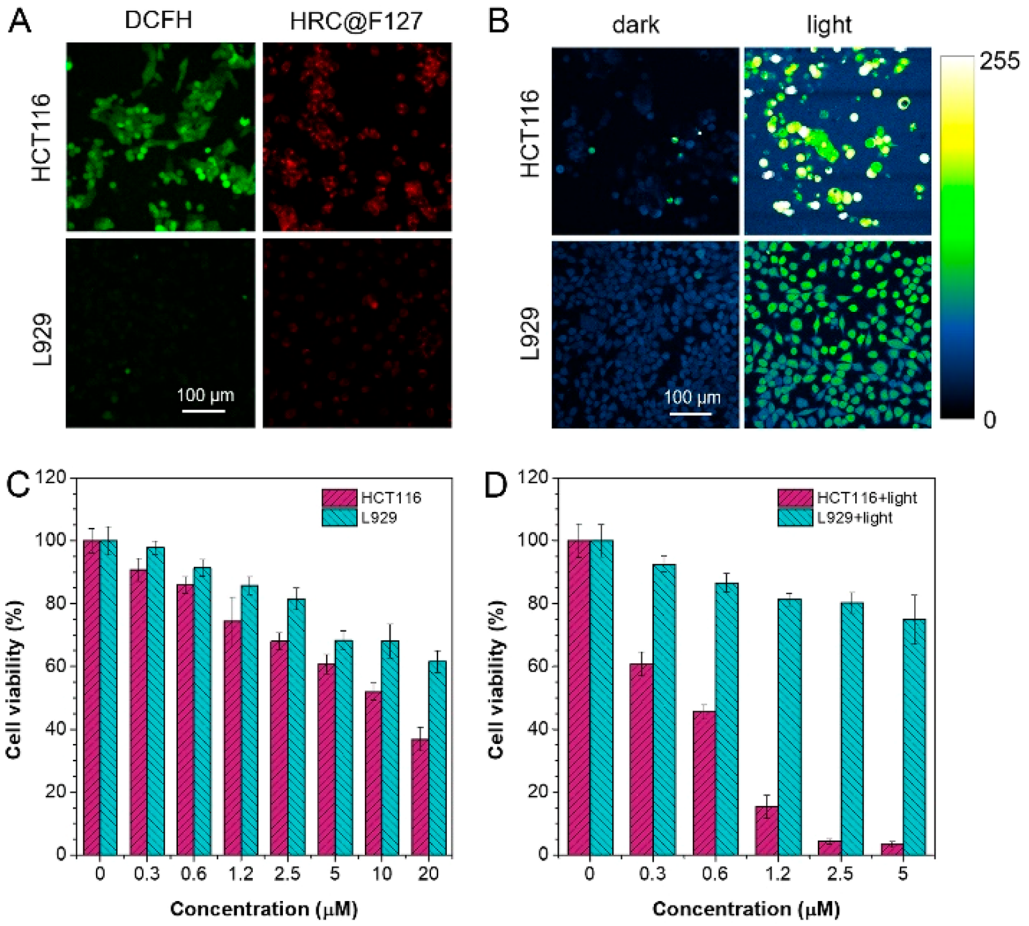

Figure 3. (A) Fluorescent images of HCT116 and L929 cells incubated with 5 μM DCFH-DA for 1 h. Ex = 488 nm. HCT116 and L929 Cells were incubated with 5 μM HRC@F127 or HCC@F127 for 24 h. Ex = 561 nm. (B) Fluorescent images of HCT116 cells and L929 cells incubated with 2 μM HRC@F127 for 24 h and 5 μM DCFH-DA for 1 h and then treated with/without 5 min light irradiation (15 mW/cm^2). Ex = 488 nm. (C, D) Cell viability of HCT116 and L929 evaluated by the MTT assay. Cells were incubated with different concentrations of HRC for 48 h (C) without or (D) with treatment with 671 nm light irradiation (light intensity = 15 mW/cm^2) for 5 min at the time point of 24 h.

higher green fluorescence intensity of the ROS indicator (Figure 2C). The elevated ROS in cells would oxidize the lipids, proteins, and DNA nearby and lead to cell malfunction and death.[58−63] The thiazolyl blue tetrazolium bromide (MTT) assay results showed that HRC had more potent cytotoxicity than HCC both in the dark and with light irradiation due to the activation by ROS. In the dark, the 50% inhibition concentration (IC_{50}) for HRC was 9.48 μM, 5-fold lower than that of HCC (47.8 μM), suggesting that CPT was effectively released by ROS activation and exhibited cytotoxicity. With light irradiation, the IC_{50} of HRC was further decreased to 0.46 μM, which was 22-fold lower than that of HCC (10.2 μM). The much lower IC_{50} suggested HRC was cleaved by ROS, and free CPT and HPPH molecules were efficiently released from the nanoparticles and killed cells effectively and synergistically with light irradiation.

Since a higher ROS level is a hallmark of cancer cells, we further tested whether HRC@F127 has selectivity toward cancer cells. To confirm this, first, the endogenous ROS levels on cancer cells (HCT116 cells) and normal cells (mouse fibroblast cell line L929) were evaluated by the ROS indicator 2′,7′-dichlorofluorescin diacetate (DCFH-DA).[39] Both live cell imaging and flow cytometry results suggested that the endogenous ROS levels in HCT116 cancer cells were much higher than those in L929 cells (Figures 3A and S12A). Then, we incubated the cells with HRC@F127 and analyzed the fluorescence recovery of HPPH molecules by fluorescence imaging (Figure 3A) and flow cytometry (Figure S12B). HCT116 cells showed a higher fluorescence intensity than L929, indicating more HPPH was released in cancer cells due to the higher ROS levels. It should be noted that though previous experiments were performed at the time point of 24 h, the difference of HCT116 and L929 cells can also be obviously observed at earlier time points (<6 h), and the difference is enlarged with time (Figure S12C). Meanwhile, fluorescence images of cells incubated with HPPH@F127 or HCC@F127 did not show a difference between HCT116 and L929 cells (Figure S13). The higher fluorescence intensity in both cell lines treated with HPPH@F127 should be attributed to the much easier release of HPPH from the particles. Overall, all these results strongly confirmed the importance of the activation by ROS in differentiating the cancer cells and normal cells.

As expected, HCT116 cells with HRC@F127 treatment and light irradiation had much higher fluorescence intensity from the ROS indicator than L929 under the same condition, not to mention those cells in the dark (Figure 3B). To evaluate the cytotoxicity, we performed the MTT assays (Figure 3C and D). Figure 3C showed a difference in cell viability between HCT116 and L929 in the dark (1.6-fold, 37% *vs* 61% at 20 μM). With light irradiation, the difference was greatly increased (19-fold, 4.3% for HCT116 *vs* 80% for L929 at 2.5 μM, Figure 3D), indicating a

https://dx.doi.org/10.1021/acsnano.0c05722
ACS Nano XXXX, XXX, XXX−XXX

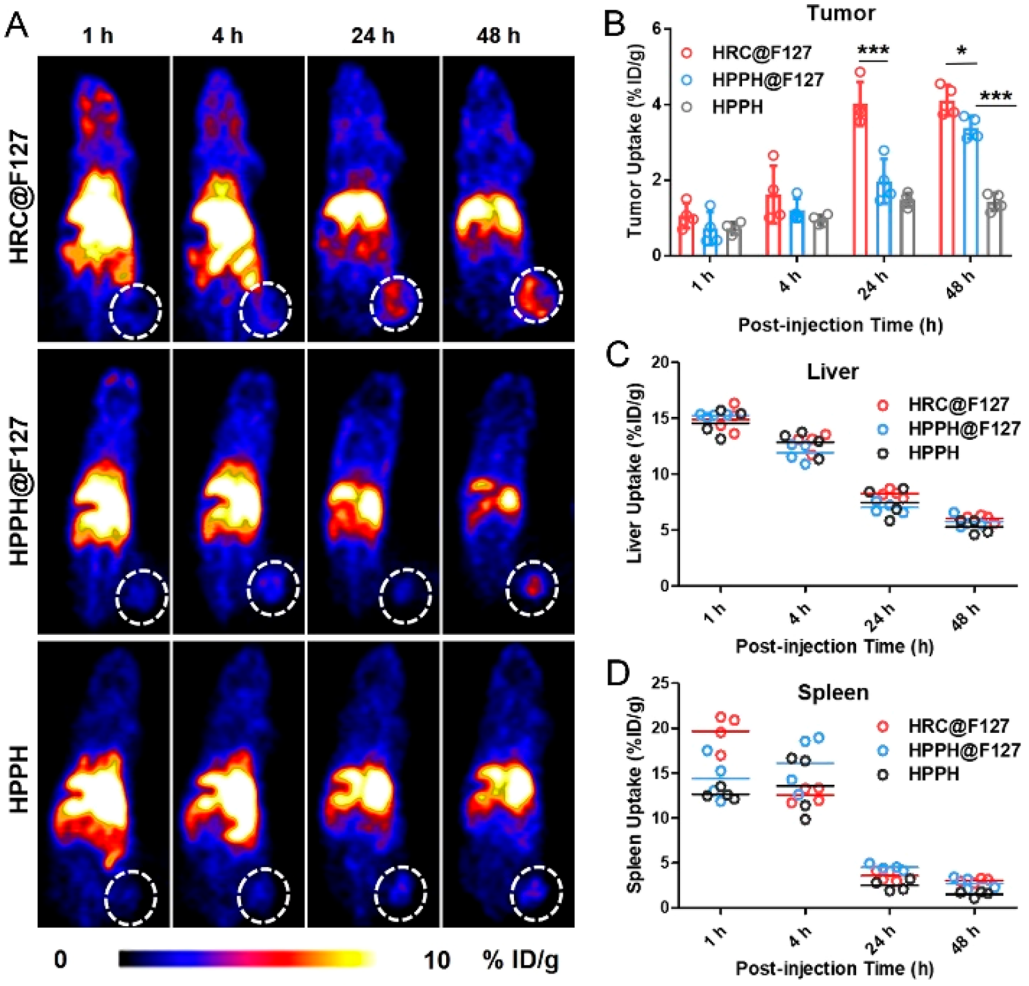

Figure 4. ***In vivo*** **distribution of HRC@F127, HPPH@F127, and HPPH molecules. (A) Representative PET images of HCT116 tumor-bearing mice at 1, 4, 24, and 48 h p.i. of ^{64}Cu-labeled HPPH-based formulation. Quantitative ROI assay of (B) tumor uptake, (C) liver uptake, and (D) spleen uptake at 1, 4, 24, and 48 h p.i. of the indicated formulation (n = 4). *P < 0.05, **P < 0.01, ***P < 0.001.**

high selectivity to kill cancer cells. In addition to HCT116 and L929 cells, we also investigated the cytotoxicity of HRC toward macrophage RAW 264.7 cells. As expected, RAW 264.7 cells exhibited a higher tolerance to the treatment (more than 70% cell viability at 2.5 μM) due to the lower ROS level (Figure S14). Above all, thanks to the higher ROS levels in cancer cells, more HRC was cleaved and more HPPH and CPT were released from the particles in cancer cells, resulting in high selectivity in cancer cell imaging and chemo- and photodynamic therapy.

In Vivo **PET Imaging and Fluorescence Imaging.** Prior to the use of this nanotheranostics for *in vivo* tumor inhibition, the biocompatibility, pharmacokinetics, and biodistribution in mice should be first studied. The hemolysis test suggested that HRC@F127 at a high concentration of 100 μg/mL only induced slight hemolysis (Figure S15), suggesting its good biocompatibility. Then, the pharmacokinetic profile (Figure S16) showed that HRC@F127 NPs had much longer retention in blood compared to HPPH molecules, further confirming the advantage of the nanoformulation. Later, using the subcutaneous xenograft human colon cancer tumor model, we further studied the biodistribution of HRC@F127 in mice by PET imaging. As the porphyrin-like structure of HPPH could coordinate with transition metals,[31,34] we labeled the free HPPH molecules, HPPH@F127 NPs, and HRC@F127 NPs with radioactive ^{64}Cu to monitor their distribution *in vivo* by quantitative PET imaging. As shown in Figure 4A, both HPPH@F127 and HRC@F127 were able to gradually accumulate in the tumor areas, while negligible PET signals were detected in mice treated with free HPPH molecules, evidencing that the F127-modified micelles exerted an enhanced permeability and retention (EPR) effect and slower body clearance for efficient drug delivery.[57] Further quantitative analysis of the region of interest (ROI) indicated that the tumor accumulation of HRC@F127 reached 4.02 ± 0.58% ID/g at 24 h postinjection (p.i.) and remained high at 48 h (4.12 ± 0.41% ID/g), which were both higher than those of HPPH@F127 NPs at the 24 h (1.98 ± 0.59% ID/g) and 48 h time point (3.39 ± 0.30% ID/g) (Figure 4B). The higher tumor uptake of HRC@F127 over HPPH@F127 was probably attributed to the lower premature drug leakage during the blood circulation and higher retention of more hydrophobic activatable prodrug HRC in the tumor. In addition to the tumor uptake, the distributions in the liver and spleen were also compared, and the results showed that they exhibited a similar trend after 24 h and could be eliminated from liver and spleen over time (Figure 4C and D), exhibiting less long-term toxicity concern.

After verification of the successful tumor accumulation of HRC@F127 by PET imaging, we subsequently evaluated whether the HRC@F127 could be activated by the tumor and the quenched fluorescence could be recovered *in vivo*. In

https://dx.doi.org/10.1021/acsnano.0c05722
ACS Nano XXXX, XXX, XXX−XXX

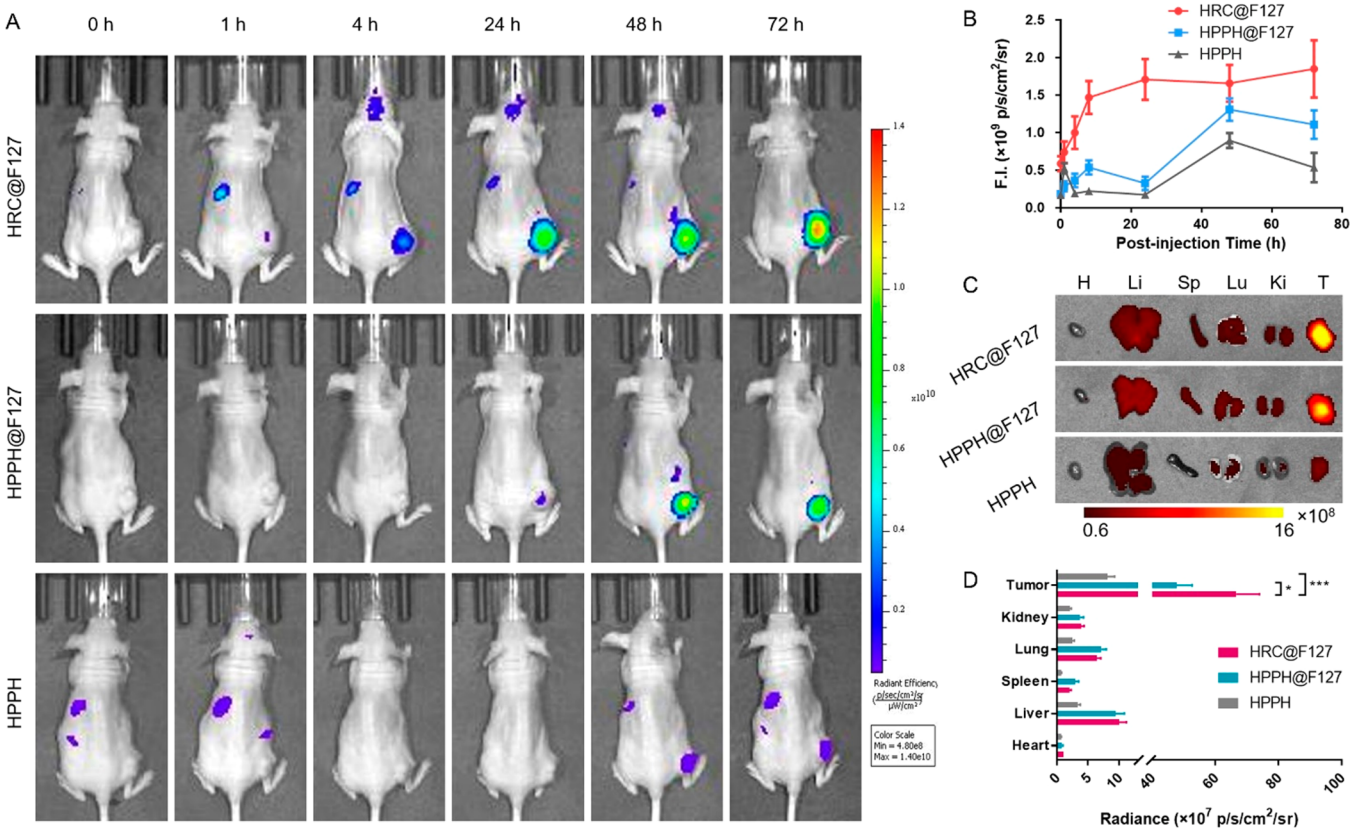

Figure 5. *In vivo* fluorescence imaging. (A) Representative *in vivo* fluorescence images of tumor-bearing mice at 1, 4, 24, and 48 h p.i. of HRC@F127, HPPH@F127, and HPPH molecules (n = 3). (B) Quantitative ROI assay of the fluorescence intensity in a tumor at designated time points after indicated treatments. (C) *Ex vivo* fluorescence images and (D) quantification of major organs from HCT116 tumor-bearing mice at 72 h p.i. H: heart, Li: liver, Sp: spleen, Lu: lung, Ki: kidney, T: tumor. *P < 0.05, **P < 0.01, ***P < 0.001.

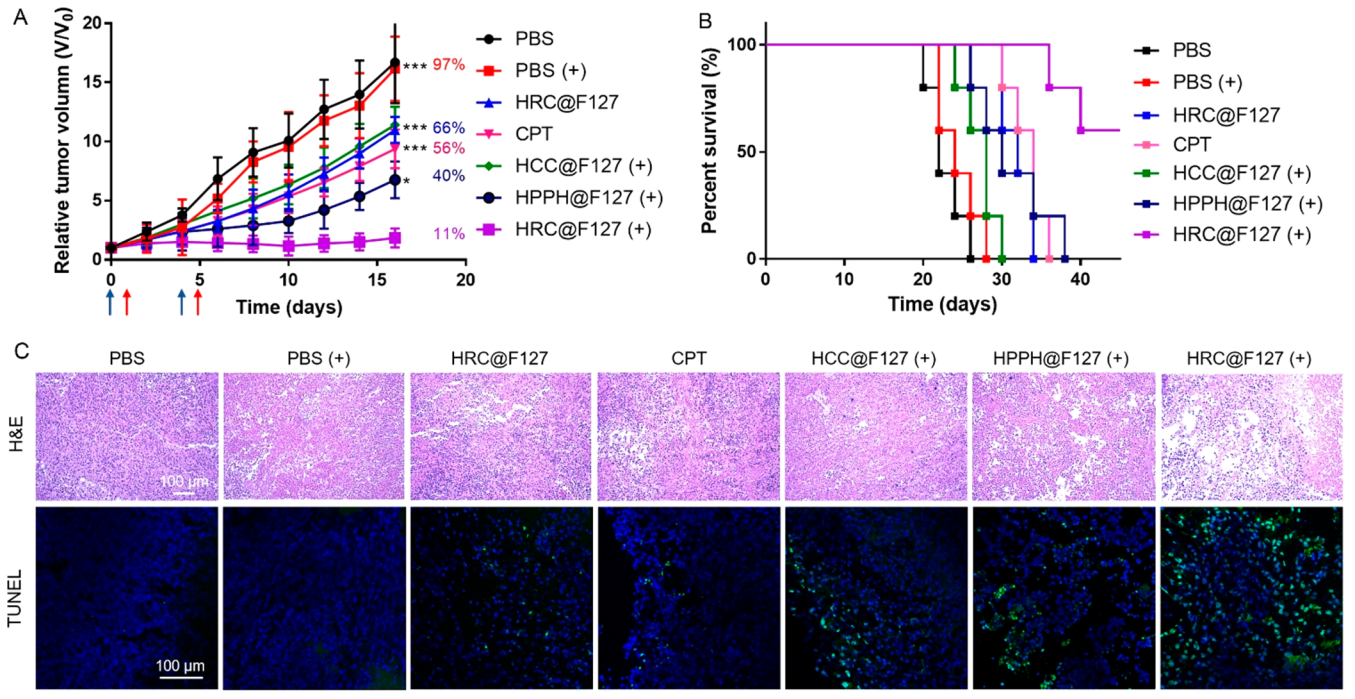

Figure 6. *In vivo* anticancer therapy. (A) Relative tumor growth curves of mice subjected to various treatments. Blue arrows indicate i.v. injection of drugs, and red arrows indicate laser irradiation. The overall tumor inhibition rates are presented after each curve. (B) Survival curves of HCT116 tumor-bearing mice after indicated treatments (n = 5). (C) H&E (upper panel) and TUNEL (lower panel) staining of tumor slices with various treatments. Blue signals: Hoechst dye H33342 (nuclear stain). Green signals: TUNEL-positive cells. Scale bar = 100 μm. *P < 0.05, **P < 0.01, ***P < 0.001.

https://dx.doi.org/10.1021/acsnano.0c05722
ACS Nano XXXX, XXX, XXX−XXX

agreement with PET results, obvious time-dependent increases of fluorescence signals in the tumor were observed in both HPPH@F127 and HRC@F127 treatment groups, while subtle signal changes were detected in the HPPH-treated mice group (Figure 5A). The HRC@F127 is expected to show minimal fluorescence until the micelle gradually dissociates, followed by the recovery of the fluorescence signal. Semiquantitative analysis revealed that the fluorescence intensity in the tumor area at 24 h after intravenous (i.v.) injection of HRC@F127 was rather high and the signal remained high up to 72 h (Figure 5B). Consistent with the PET imaging results, the fluorescence intensity of HPPH@F127 reached a peak value at 48 h and was close to that of HRC@F127 at 48 h. This result provides strong evidence that HRC@F127 could undergo "off-to-on" transition, and most fluorescence was recovered at the tumor site. More importantly, HPPH@F127 showed much slower tumor light-up and faster signal decrease compared to HRC@F127, which might be attributed to its faster drug leakage and slower tumor accumulation. Additionally, the *ex vivo* biodistribution in major organs at 72 h after different treatments clearly revealed preferential retention of HRC@F127 over HPPH@F127 and HPPH molecules at tumor sites, while other major organs presented much lower signals (Figure 5C and D), indicating the high selectivity of HRC@F127 for tumors and thus benefiting the reduction of potential side effects. Overall, PET and fluorescence imaging results clearly demonstrated that HRC@F127 could preferentially accumulate in tumor sites with prolonged retention and efficient fluorescence recovery.

***In Vivo* Anticancer Activity in a Mouse Model.** Encouraged by the promising *in vitro* cytotoxicity and *in vivo* tumor accumulation results of HRC@F127 NPs, we further explored their therapeutic effect on an established subcutaneous xenograft tumor model of human colon cancer in athymic nude mice. HCT116 tumor-bearing mice were randomly divided into 7 groups (n = 5/group) and intravenously treated with the following regimens: G1 (PBS), G2 (PBS, + laser), G3 (HRC@F127), G4 (CPT), G5 (HCC@F127 + laser), G6 (HPPH@F127 + laser), and G7 (HRC@F127 + laser). The mice were treated with two doses at an interval of 4 days, and the groups with laser treatment were irradiated at the tumor region using a 671 nm laser at 24 h p.i. (10 min, 100 mW/cm^2). As seen in Figure 6A, mice injected with PBS with or without laser irradiation exhibited fast tumor growth. G3 (HRC@F127) with the ability of endogenous ROS-responsive drug release and G4 (CPT) could moderately cause 56% and 66% tumor inhibition on day 16, which was probably attributed to the individual chemotherapy effect. When exposed to laser irradiation, the tumor treated with HRC@F127 was significantly suppressed, which is much more effective than the G5 group (HCC@F127 + laser) without drug release and limited PDT effect. For the G6 (HPPH@F127 + laser) group, although the PDT effect contributed to around 40% tumor inhibition, the "always on" PDT platform without tumor selectivity could display potential side effects and the mice must always be kept in a dark place (low percent survival, Figure 6B). On the contrary, the G7 (HRC@F127 + laser)-treated mice would not suffer from light exposure-induced systemic toxicity during the whole period of treatment, further manifesting the importance of the ROS-activatable "off−on" PDT and chemotherapy. Moreover, the G7 treatment group provided the best overall survival over the other groups, owing to its desirable synergistic therapeutic outcome (Figure 6B). To further elucidate the underlying mechanism, hematoxylin and eosin (H&E) and terminal deoxynucleotidyl transferase deoxyuridine triphosphate (dUTP) nick end labeling (TUNEL) staining were performed in tumor tissues after various treatments (Figure 6C, upper and lower panels, respectively). In line with the trend of *in vivo* tumor inhibition, there was an obvious hiatus in the cell spaces, nuclei shrinkage by H&E results, and enhanced cell apoptosis in the HRC@F127 + laser group compared to the other treatment groups. Besides an antitumor effect, the safety of the designed nanoparticle is of concern for further clinical translation and was thus assessed with two key important factors (body weight and major organ injury). As shown in Figures S17 and S18), there was no obvious body weight loss or injury to major organs during the treatment course of HRC@F127 + laser as compared to the control groups, suggesting HRC@F127 had minimal side effects. Taken together, the nanoparticles of the designed ROS-sensitive heterodimer prodrug could largely overcome the off-target risk and improve the anticancer efficacy and could be considered as an ideal candidate for *in vivo* anticancer therapy.

CONCLUSION

In summary, we have designed and prepared a ROS-activatable heterodimeric prodrug of a synergistic drug pair (CPT and HPPH) *via* a thioketal linker for tumor-selective imaging and therapy. The prodrug was able to be efficiently encapsulated into a biocompatible polymeric nanocarrier with higher loading capacity, better colloidal stability, and much lower premature drug leakage than their corresponding monomeric drug-loaded NPs. After formation of the nanotheranostics in aqueous solutions, HRC tends to form aggregates due to the strong $\pi-\pi$ stacking and its fluorescence was thus quenched. Upon cleavage by endogenous ROS in cells, the HPPH and CPT segments of HRC were released from the NPs, lit up the cells, and exhibited cytotoxicity to the cells through synergistic chemotherapy and photodynamic therapy. Due to the higher ROS levels in cancer cells than normal cells, HRC@F127 could selectively light up the cancer cells and exhibit much more potent cytotoxicity to cancer cells. The *in vivo* results indicated that HRC@F127 demonstrated effective tumor accumulation and synergistic therapeutic efficacy with longer survival and minimal side effects on mice. Above all, our results clearly demonstrate that nanotheranotics based on the ROS-activable heterodimeric prodrug HRC is a promising approach for safe delivery of antitumor drugs and improving cancer therapeutic efficacy. Such a simple formulation and the defined small molecular structure will be of benefit for future clinical translation.

EXPERIMENTAL SECTION

Materials and Instruments. (*S*)-(+)-Camptothecin was purchased from Fisher Scientific. 2-(1-Hexyloxyethyl)-2-devinyl pyropheophorbide-α was purchased from MedKoo Biosciences. All other chemicals and solvents were purchased from Sigma-Aldrich and used without further purification. The ^{1}H NMR spectra were performed with a Bruker AV300 spectrometer (300 MHz), and chemical shifts were referenced to the solvent residual signals or internal standard tetramethylsilane. UV−vis absorption spectra were recorded by a UV3100PC spectrophotometer (VWR). DLS measurements were determined by a Horiba SZ-100 instrument. Photoluminescence spectra were obtained by a Hitachi F-7000 fluorescence spectrophotometer. The control compound HCC with an uncleavable were synthesized in a previous report.[34]

Synthesis of Compound 1. As shown in Scheme S1, the precursor of compound **1** was synthesized from the condensation of methyl thioglycolate (70 mmol, 6.26 mL) and acetone (34 mmol, 2.55 mL)

https://dx.doi.org/10.1021/acsnano.0c05722
ACS Nano XXXX, XXX, XXX−XXX

under the catalysis of BF_3Et_2O (110 mmol, 13 mL) in 50 mL of acetonitrile according to the literature report.[64] The compound was obtained as a pale yellow oil (yield: 90%). ^{1}H NMR (300 MHz, MeOD): δ_H (ppm) 3.718 (6H, s), 3.463 (4H, s), 1.603 (6H, s). Referring to the literature,[48] the precursor of compound **1** (1 g) in anhydrous THF (150 mL) was cooled in an ice bath, and $LiAlH_4$(1 g) (1.52 g, 40.1 mmol) was slowly added into the reaction mixture. After 30 min, the mixture was slowly heated to reflux for 2 h and quenched by water (1 mL). The mixture was filtered, and the solvent of the filtrate was evaporated to dryness by rotatory evaporator to obtain a yellow liquid. The liquid was purified by silica column chromatography at 5% MeOH/DCM to give the product as a yellow liquid, compound **1** (yield: 98%). ^{1}H NMR (300 MHz, $CDCl_3$): δ_H (ppm) 3.67 (4H, t, J = 6 Hz), 3.54 (2H, s), 2.75 (4H, t, J = 6 Hz), 1.53 (6H, s).

Synthesis of Compound 2. Referring to the method in the literature,[48] CPT (348 mg, 1 mmol) and DMAP (240 mg, 2 mmol) were stirred in 40 mL of dry CH_2Cl_2 and cooled in an ice bath under N_2 protection. Triphosgene (100 mg, 0.33 mmol) was added to the mixture, and reaction mixture was stirred for 30 min at room temperature. Subsequently, compound **1** (800 mg, 4 mmol) dissolved in dry tetrahydrofuran (10 mL) was added, and the reaction mixture was stirred overnight. The reaction was filtered, and the solvent was removed with a rotatory evaporator. The crude product was purified by column chromatography to give the CPT prodrug, compound **2**, as a pale white solid (yield: 80%). ^{1}H NMR (300 MHz, MeOD): δ_H (ppm) 8.42 (1H, s, CPT), 8.24 (1H, d, J = 8.4 Hz, CPT), 7.95 (1H, d, J = 8.1 Hz, CPT), 7.85 (1H, t, J = 7.7 Hz, CPT), 7.69 (1H, t, J = 7.5 Hz, CPT), 7.39 (1H, s, CPT), 5.70 (1H, d, J = 17.4 Hz, CPT), 5.42−5.29 (3H, m, CPT), 4.23 (2H, t, J = 7.0 Hz), 3.70 (2H, t, J = 6.0 Hz), 2.86−2.74 (4H, m, thioketal linker), 2.28−2.03 (2H, m, CPT), 1.47 (6H, s, methyl groups of thioketal linker), 0.93 (3H, t, J = 7.5 Hz, CPT).

Synthesis of HRC. HPPH (12.6 mg, 0.02 mmol), **2** (14 mg, 0.025 mmol), DMAP (0.6 mg, 0.5 mmol), and EDC·HCl (9 mg, 0.05 mmol) were dissolved and stirred in 5 mL of CH_2Cl_2 at room temperature for 24 h. Then the mixture was concentrated by rotatory evaporator and purified by silica column using ethyl acetate/hexane as eluent. Yield: 70%. Chemical formula: $C_{67}H_{76}N_6O_{10}S_2$. ^{1}H NMR (300 MHz, $CDCl_3$): δ_H (ppm) 9.75 (1H, d, J = 8.1 Hz, CPT), 9.46 (1H, s, CPT), 8.36 (1H, d, J = 9.7 Hz, CPT), 7.89 (1H, t, J = 10 Hz, CPT), 7.55−7.47 (2H, m, CPT), 7.28−7.20 (3H, m), 7.12 (1H, d, J = 9.6 Hz), 5.98−5.93 (1H, m), 5.73 (1H, d, J = 17.1 Hz), 5.43−5.25 (1H, m), 5.23−5.02 (2H, m), 4.87−4.61 (2H, m), 4.48−4.12 (6H, m), 3.80−3.60 (6H, m), 3.39 (3H, d, J = 4.8 Hz), 3.33 (3H, s), 2.93−2.76 (4H, m, thioketal linker), 2.50−2.07 (6H, m), 1.95−1.65 (10H, m), 1.53 (6H, s, methyl groups of thioketal linker), 1.36−1.20 (8H, m), 1.01−0.78 (6H, m), −1.86 (1H, d, J = 14.4 Hz). ESI-MS m/z (M^+): calc 1188.5064, found ($M + H^+$) 1189.5490.

Nanoformulation with Pluronic F127 Polymer. The nanoparticles were obtained through a nanoprecipitation method. Briefly, HRC, HCC, HPPH, or CPT was dissolved in DMSO at a concentration of 5 mM. A 40 μL amount of the solution was first mixed with 50 μL of F127 (20 mg/mL in DMSO) solution. Then 910 μL of water was added into the solution and mixed thoroughly. The unencapsulated free molecules and DMSO were removed by centrifuge dialysis (30 kDa). When the solution in the centrifuge tube was less than 100 μL, water was added to resuspend the nanoparticles and make up a solution volume of 1 mL (<1% DMSO remaining). The solutions were filtered with a 220 nm filter to remove the possible drug aggregates. The amount of drug before and after dialysis and filtration was measured by UV−vis absorbance to calculate the drug loading efficiency (drug loading efficiency = $A_{after}/A_{before} \times 100\%$).

Drug Leakage Measured by a Dialysis Method. Briefly, 1 mL of the diluted solution of CPT@F127, HPPH@F127, or HRC@F127 (diluted with phosphate-buffered saline (PBS) to a drug concentration of 80 μM) was transferred into a semipermeable membrane tubing (MWCO: 10 kDa) and dialyzed against 30 mL of PBS in a beaker covered with foil paper at room temperature. At different time points, 2 mL of the solution was collected from the beaker, and 2 mL of fresh PBS was added. At the end point, the amount of drug left in the dialysate was measured by UV−vis absorption. For CPT, the cumulative release curve was obtained by measuring the CPT concentration in the collected solutions at each time point. The diluted CPT concentration was determined by the fluorescence method with a calibration curve. Each experimental group was evaluated in duplicate.

Cell Viability Evaluated by MTT Assays. HCT116, L929, or RAW 264.7 cells were cultured with completed DMEM (containing 10% fetal bovine serum, 100 IU/mL penicillin, and 100 μg/mL streptomycin) in a 37 °C incubator with an air atmosphere containing 5% CO_2. The passage was performed every 2 to 3 days. For the MTT assay, cells were seeded in 96-well plates at the density of 5000 cells/well for 24 h and then incubated with 100 μL of fresh completed medium containing drugs (CPT and HPPH) or drug-loaded nanoparticles (HRC@F127 or HCC@F127) at predetermined concentrations. For dark toxicity, cells were incubated with drugs for 48 h and protected from light. For photodynamic treatment, cells were irradiated with a 671 nm laser for 5 min at 15 mW/cm^2 at the time point of 24 h and further incubated for another 24 h. Then, 10 μL of 5 mg/mL MTT in medium was added to each well and incubated for 4 h. After careful removal of the medium, 100 μL of DMSO was added to each well. Then the absorbance of each well was recorded at a wavelength of 570 nm by a BioTek Synergy H4 hybrid plate reader. After background subtraction, the cell viability of each group was calculated from the relative absorbance value to the control groups. Each group was performed with six parallel wells.

Cellular Imaging. Cell imaging was performed with an LSM780 confocal microscope. HCT116 cells were incubated with HPPH, HRC@F127, and HCC@F127 at 5 μM for 24 h and then washed with cold Dulbecco's PBS three times before imaging.

Pharmacokinetic Study. The prepared HRC@F127 NPs or free HPPH were i.v. injected into mice (n = 3), and the blood samples were collected at 5 min, 15 min, 30 min, 1 h, 4 h, and 24 h. Then blood samples were centrifuged at 4000 rpm for 5 min to collect the supernatant plasma. Methanol was added into the supernatant to extract HRC or HPPH, and the resulting mixture was incubated at 4 °C for 4 h. The methanol extract was obtained by centrifugation, and the concentration of HRC or HPPH was determined with a standard curve by the fluorescence method.

Hemolysis Assay. Red blood cells (RBCs) were isolated by centrifugation and washed and diluted with PBS before use. In the test, 0.25 mL of RBC suspension was mixed with 1 mL of HRC@F127 at various concentrations in PBS. After incubation for 3 h, samples were centrifuged, and the supernatants were collected and analyzed by UV−vis absorbance at 540 nm. Backgrounds were subtracted by control experiments, and the percentages of hemolysis were calculated and plotted.

Radioactive [^{64}Cu]-Labeling of HPPH NPs and HPPH-ROS-CPT NPs. Radioactive metal [^{64}Cu] was produced by the PET Department in the NIH Clinical Center. First, we prepared stock solutions of HRC and HPPH in DMSO at 1.0 mg/mL, respectively. Then, an aliquot of the solution (0.1 mL) was mixed with 0.1 mL of [^{64}CuOAc] in 0.4 M sodium acetate (pH = 5.6) buffer and incubated at 50 °C for 5−7 min. Then, 0.2 mL of F127 (10 mg/mL in DMSO) was added, and the solution was stirred for 30 min. Later, 0.2 mL of water was added to the mixture, and the mixture was then purified by passing through a PD-10 column using PBS as the eluent. The total time of labeling and purification procedures took about 1 h. Before the i.v. injection, the radioactivity of the radiolabeled solutions of HPPH, HPPH@F127, and HRC@F127 was diluted to 120−150 μCi (4.44−5.55 MBq) per 100 μL for use.

Fluorescence Imaging and PET Imaging of HCT116 Tumors. All animal work was conducted in accordance with the NIH Guide for the Care and Use of Animals under the protocols approved by the NIH Clinical Center Animal Care and Use Committee. HCT116 tumor-bearing nude mice (8 weeks old, female) were prepared by subcutaneous injection of HCT116 cells (5×10^6) into the flank of the athymic nude mice. When the tumor sizes reached 500−1000 mm^3, mice were used for fluorescence imaging and PET imaging. For the fluorescence imaging, 100 μL of the solutions of HPPH, HPPH@F127, and HRC@F127 (all the HPPH is 2.5 mg/kg) was intravenously injected into the HCT116 tumor-bearing mice. The fluorescent scans

https://dx.doi.org/10.1021/acsnano.0c05722
ACS Nano XXXX, XXX, XXX−XXX

were recorded at 1, 4, 24, 48, and 72 h p.i. on an IVIS Spectrum system. At 72 h postinjection, the above mice were sacrificed, and major organs were collected and imaged. For PET imaging, 100 μL of the ^{64}Cu-labeled solutions of free HPPH molecules, HPPH@F127, and HRC@F127 was i.v. injected into HCT116 tumor-bearing mice at a radioactivity of around 120−150 μCi. At 1, 4, 24, and 48 h p.i., mice were scanned on an Inveon DPET scanner. ASI Pro VMTM software was used for image analysis.

***In Vivo* Therapy in HCT116 Tumor-Bearing Mice.** HCT116 tumor-bearing nude mice (8 weeks old, female) were prepared by subcutaneous injection of a suspension of 5×10^6 HCT116 cells in PBS (100 μL). When the tumor reached around 80−100 mm mm^3 after tumor inoculation, the mice were randomly divided into seven groups ($n = 5$) and i.v. injected with specified regimens: G1 (PBS), G2 (PBS + laser), G3 (HRC@F127), G4 (CPT), G5 (HCC@F127 + laser), G6 (HPPH@F127 + laser), and G7 (HRC@F127 + laser) twice at an interval of 4 days (dose of injection: CPT: 1.7 mg/kg, HPPH: 2.5 mg/kg, HRC: 5 mg/kg, HCC: 5 mg/kg, same molar concentration). Irradiation by a 671 nm laser (100 mW/cm^2, 10 min) was performed for the noted groups at 24 h p.i. each time. Tumor volume and body weight of mice were recorded every other day. The volume was calculated using the formula volume = (length × width^2)/2. Mice were euthanized when any dimension of tumor was close to 2 cm or over 20% of the mouse body weight was lost. Results were analyzed using GraphPad Prism.

Statistical Analysis. Quantitative data were presented as mean ± SD. Statistical differences were calculated by an unpaired two-tailed Student's t test using Excel software. P values < 0.05 were considered statistically significant ($^*P < 0.05$, $^{**}P < 0.01$, $^{***}P < 0.001$).

ASSOCIATED CONTENT

Supporting Information

The Supporting Information is available free of charge at https://pubs.acs.org/doi/10.1021/acsnano.0c05722.

Detailed synthesis procedures, structural characterizations, supplementary fluorescence spectra and images, DLS results, H&E staining images, plot of body weight change, *etc.* (PDF)

AUTHOR INFORMATION

Corresponding Authors

Jing Mu − *Marshall Laboratory of Biomedical Engineering, International Cancer Center, Laboratory of Evolutionary Theranostics (LET), School of Biomedical Engineering, Shenzhen University Health Science Center, Shenzhen 518060, China; Key Laboratory of Optoelectronic Devices and Systems of Ministry of Education and Guangdong Province, College of Optoelectronic Engineering, Shenzhen University, Shenzhen 518060, China; Laboratory of Molecular Imaging and Nanomedicine (LOMIN), National Institute of Biomedical Imaging and Bioengineering (NIBIB), National Institutes of Health, Bethesda, Maryland 20892, United States;* orcid.org/0000-0002-7508-1461; Email: mujing1921@gmail.com

Peng Huang − *Marshall Laboratory of Biomedical Engineering, International Cancer Center, Laboratory of Evolutionary Theranostics (LET), School of Biomedical Engineering, Shenzhen University Health Science Center, Shenzhen 518060, China;* orcid.org/0000-0003-3651-7813; Email: peng.huang@szu.edu.cn

Xiaoyuan Chen − *Laboratory of Molecular Imaging and Nanomedicine (LOMIN), National Institute of Biomedical Imaging and Bioengineering (NIBIB), National Institutes of Health, Bethesda, Maryland 20892, United States; Yong Loo Lin School of Medicine and Faculty of Engineering, National University of Singapore, Singapore 117597 Singapore;* orcid.org/0000-0002-9622-0870; Email: chen9647@gmail.com

Authors

Meijuan Jiang − *Marshall Laboratory of Biomedical Engineering, International Cancer Center, Laboratory of Evolutionary Theranostics (LET), School of Biomedical Engineering, Shenzhen University Health Science Center, Shenzhen 518060, China; Key Laboratory of Optoelectronic Devices and Systems of Ministry of Education and Guangdong Province, College of Optoelectronic Engineering, Shenzhen University, Shenzhen 518060, China; Laboratory of Molecular Imaging and Nanomedicine (LOMIN), National Institute of Biomedical Imaging and Bioengineering (NIBIB), National Institutes of Health, Bethesda, Maryland 20892, United States;* orcid.org/0000-0002-7918-7538

Orit Jacobson − *Laboratory of Molecular Imaging and Nanomedicine (LOMIN), National Institute of Biomedical Imaging and Bioengineering (NIBIB), National Institutes of Health, Bethesda, Maryland 20892, United States*

Zhantong Wang − *Laboratory of Molecular Imaging and Nanomedicine (LOMIN), National Institute of Biomedical Imaging and Bioengineering (NIBIB), National Institutes of Health, Bethesda, Maryland 20892, United States*

Liangcan He − *Laboratory of Molecular Imaging and Nanomedicine (LOMIN), National Institute of Biomedical Imaging and Bioengineering (NIBIB), National Institutes of Health, Bethesda, Maryland 20892, United States;* orcid.org/0000-0002-9415-9535

Fuwu Zhang − *Laboratory of Molecular Imaging and Nanomedicine (LOMIN), National Institute of Biomedical Imaging and Bioengineering (NIBIB), National Institutes of Health, Bethesda, Maryland 20892, United States*

Weijing Yang − *Laboratory of Molecular Imaging and Nanomedicine (LOMIN), National Institute of Biomedical Imaging and Bioengineering (NIBIB), National Institutes of Health, Bethesda, Maryland 20892, United States*

Qiaoya Lin − *Laboratory of Molecular Imaging and Nanomedicine (LOMIN), National Institute of Biomedical Imaging and Bioengineering (NIBIB), National Institutes of Health, Bethesda, Maryland 20892, United States*

Zijian Zhou − *Laboratory of Molecular Imaging and Nanomedicine (LOMIN), National Institute of Biomedical Imaging and Bioengineering (NIBIB), National Institutes of Health, Bethesda, Maryland 20892, United States*

Ying Ma − *Laboratory of Molecular Imaging and Nanomedicine (LOMIN), National Institute of Biomedical Imaging and Bioengineering (NIBIB), National Institutes of Health, Bethesda, Maryland 20892, United States*

Jing Lin − *Marshall Laboratory of Biomedical Engineering, International Cancer Center, Laboratory of Evolutionary Theranostics (LET), School of Biomedical Engineering, Shenzhen University Health Science Center, Shenzhen 518060, China;* orcid.org/0000-0001-9865-2098

Junle Qu − *Key Laboratory of Optoelectronic Devices and Systems of Ministry of Education and Guangdong Province, College of Optoelectronic Engineering, Shenzhen University, Shenzhen 518060, China*

Complete contact information is available at: https://pubs.acs.org/10.1021/acsnano.0c05722

https://dx.doi.org/10.1021/acsnano.0c05722
ACS Nano XXXX, XXX, XXX−XXX

Notes

The authors declare no competing financial interest.

ACKNOWLEDGMENTS

This work is financially supported by the National Key R&D Program of China (2018YFA0704000), Basic Research Program of Shenzhen (JCYJ20170412111100742, JCYJ201805-07182413022, JCYJ20180305163622079), Fok Ying-Tong Education Foundation for Young Teachers in the Higher Education Institutions of China (161032), Guangdong Province Natural Science Foundation of Major Basic Research and Cultivation Project (2018B030308003), Shenzhen Science and Technology Program (KQTD20190929172538530), and the Intramural Research Program and National Institute of Biomedical Imaging and Bioengineering, National Institutes of Health (NIH). We thank the Instrumental Analysis Center of Shenzhen University (Lihu Campus). We thank the National Institute of Child Health and Human Development Microscopy & Imaging Core, specifically, V. Schram and L. Holtzclaw for their technical support. We thank the the U.S. National Heart Lung and Blood Institute (NHLBI) electron microscopy core, specifically, P. Anand for assistance during the EM acquisition and analyses.

REFERENCES

(1) Markman, J. L.; Rekechenetskiy, A.; Holler, E.; Ljubimova, J. Y. Nanomedicine Therapeutic Approaches to Overcome Cancer Drug Resistance. *Adv. Drug Delivery Rev.* **2013**, *65*, 1866−1879.

(2) Fan, W.; Yung, B.; Huang, P.; Chen, X. Nanotechnology for Multimodal Synergistic Cancer Therapy. *Chem. Rev.* **2017**, *117*, 13566−13638.

(3) Hu, Q.; Sun, W.; Wang, C.; Gu, Z. Recent Advances of Cocktail Chemotherapy by Combination Drug Delivery Systems. *Adv. Drug Delivery Rev.* **2016**, *98*, 19−34.

(4) Bildstein, L.; Dubernet, C.; Couvreur, P. Prodrug-Based Intracellular Delivery of Anticancer Agents. *Adv. Drug Delivery Rev.* **2011**, *63*, 3−23.

(5) PeiróCadahía, J.; Previtali, V.; Troelsen, N. S.; Clausen, M. H. Prodrug Strategies for Targeted Therapy Triggered by Reactive Oxygen Species. *MedChemComm* **2019**, *10*, 1531−1549.

(6) Han, H.-K.; Amidon, G. L. Targeted Prodrug Design to Optimize Drug Delivery. *AAPS PharmSci* **2000**, *2*, 48−58.

(7) Yao, X.; Mu, J.; Zeng, L.; Lin, J.; Nie, Z.; Jiang, X.; Huang, P. Stimuli-Responsive Cyclodextrin-Based Nanoplatforms for Cancer Treatment and Theranostics. *Mater. Horiz.* **2019**, *6*, 846−870.

(8) Kim, H.; Kwak, G.; Kim, K.; Yoon, H. Y.; Kwon, I. C. Theranostic Designs of Biomaterials for Precision Medicine in Cancer Therapy. *Biomaterials* **2019**, *213*, 119207.

(9) Goel, S.; Ferreira, C. A.; Chen, F.; Ellison, P. A.; Siamof, C. M.; Barnhart, T. E.; Cai, W. Activatable Hybrid Nanotheranostics for Tetramodal Imaging and Synergistic Photothermal/Photodynamic Therapy. *Adv. Mater.* **2018**, *30*, 1704367.

(10) Sharma, A.; Lee, M.-G.; Won, M.; Koo, S.; Arambula, J. F.; Sessler, J. L.; Chi, S.-G.; Kim, J. S. Targeting Heterogeneous Tumors Using a Multifunctional Molecular Prodrug. *J. Am. Chem. Soc.* **2019**, *141*, 15611−15618.

(11) Lee, M. H.; Sharma, A.; Chang, M. J.; Lee, J.; Son, S.; Sessler, J. L.; Kang, C.; Kim, J. S. Fluorogenic Reaction-Based Prodrug Conjugates as Targeted Cancer Theranostics. *Chem. Soc. Rev.* **2018**, *47*, 28−52.

(12) Su, H.; Zhang, P.; Cheetham, A. G.; Koo, J. M.; Lin, R.; Masood, A.; Schiapparelli, P.; Quiñones-Hinojosa, A.; Cui, H. Supramolecular Crafting of Self-Assembling Camptothecin Prodrugs with Enhanced Efficacy against Primary Cancer Cells. *Theranostics* **2016**, *6*, 1065−1074.

(13) Saravanakumar, G.; Kim, J.; Kim, W. J. Reactive-Oxygen-Species-Responsive Drug Delivery Systems: Promises and Challenges. *Adv. Sci.* **2017**, *4*, 1600124.

(14) Ye, H.; Zhou, Y.; Liu, X.; Chen, Y.; Duan, S.; Zhu, R.; Liu, Y.; Yin, L. Recent Advances on Reactive Oxygen Species-Responsive Delivery and Diagnosis System. *Biomacromolecules* **2019**, *20*, 2441−2463.

(15) Zhou, Z.; Ni, K.; Deng, H.; Chen, X. Dancing with Reactive Oxygen Species Generation and Elimination in Nanotheranostics for Disease Treatment. *Adv. Drug Deliver. Rev.* 2020, DOI: 10.1016/j.addr.2020.06.006.

(16) Trachootham, D.; Alexandre, J.; Huang, P. Targeting Cancer Cells by ROS-Mediated Mechanisms: A Radical Therapeutic Approach? *Nat. Rev. Drug Discovery* **2009**, *8*, 579−591.

(17) Fan, W.; Huang, P.; Chen, X. Overcoming the Achilles' Heel of Photodynamic Therapy. *Chem. Soc. Rev.* **2016**, *45*, 6488−6519.

(18) Ballance, W. C.; Qin, E. C.; Chung, H. J.; Gillette, M. U.; Kong, H. Reactive Oxygen Species-Responsive Drug Delivery Systems for the Treatment of Neurodegenerative Diseases. *Biomaterials* **2019**, *217*, 119292.

(19) Zhou, F. Y.; Feng, B.; Wang, T. T.; Wang, D. G.; Cui, Z. R.; Wang, S. L.; Ding, C. Y.; Zhang, Z. W.; Liu, J.; Yu, H. J.; Li, Y. P. Theranostic Prodrug Vesicles for Reactive Oxygen Species-Triggered Ultrafast Drug Release and Local-Regional Therapy of Metastatic Triple-Negative Breast Cancer. *Adv. Funct. Mater.* **2017**, *27*, 12.

(20) Xu, X.; Saw, P. E.; Tao, W.; Li, Y.; Ji, X.; Bhasin, S.; Liu, Y.; Ayyash, D.; Rasmussen, J.; Huo, M.; Shi, J.; Farokhzad, O. C. ROS-Responsive Polyprodrug Nanoparticles for Triggered Drug Delivery and Effective Cancer Therapy. *Adv. Mater.* **2017**, *29*, 1700141.

(21) Pei, P.; Sun, C.; Tao, W.; Li, J.; Yang, X.; Wang, J. ROS-Sensitive Thioketal-Linked Polyphosphoester-Doxorubicin Conjugate for Precise Phototriggered Locoregional Chemotherapy. *Biomaterials* **2019**, *188*, 74−82.

(22) Wang, S.; Wang, Z.; Yu, G.; Zhou, Z.; Jacobson, O.; Liu, Y.; Ma, Y.; Zhang, F.; Chen, Z.-Y.; Chen, X. Tumor-Specific Drug Release and Reactive Oxygen Species Generation for Cancer Chemo/Chemodynamic Combination Therapy. *Adv. Sci.* **2019**, *6*, 1801986.

(23) Wang, S.; Yu, G.; Wang, Z.; Jacobson, O.; Lin, L. S.; Yang, W.; Deng, H.; He, Z.; Liu, Y.; Chen, Z. Y. Enhanced Antitumor Efficacy by a Cascade of Reactive Oxygen Species Generation and Drug Release. *Angew. Chem.* **2019**, *131*, 14900−14905.

(24) Yuan, Y.; Liu, J.; Liu, B. Conjugated-Polyelectrolyte-Based Polyprodrug: Targeted and Image-Guided Photodynamic and Chemotherapy with On-Demand Drug Release upon Irradiation with a Single Light Source. *Angew. Chem., Int. Ed.* **2014**, *53*, 7163−7168.

(25) Zhou, Q.; Shao, S.; Wang, J.; Xu, C.; Xiang, J.; Piao, Y.; Zhou, Z.; Yu, Q.; Tang, J.; Liu, X.; Gan, Z.; Mo, R.; Gu, Z.; Shen, Y. Enzyme-Activatable Polymer-Drug Conjugate Augments Tumour Penetration and Treatment Efficacy. *Nat. Nanotechnol.* **2019**, *14*, 799−809.

(26) Elsabahy, M.; Wooley, K. L. Design of Polymeric Nanoparticles for Biomedical Delivery Applications. *Chem. Soc. Rev.* **2012**, *41*, 2545−2561.

(27) Cai, K.; He, X.; Song, Z.; Yin, Q.; Zhang, Y.; Uckun, F. M.; Jiang, C.; Cheng, J. Dimeric Drug Polymeric Nanoparticles with Exceptionally High Drug Loading and Quantitative Loading Efficiency. *J. Am. Chem. Soc.* **2015**, *137*, 3458−3461.

(28) Guo, X.; Wang, L.; Duval, K.; Fan, J.; Zhou, S.; Chen, Z. Dimeric Drug Polymeric Micelles with Acid-Active Tumor Targeting and FRET-Traceable Drug Release. *Adv. Mater.* **2018**, *30*, 1705436.

(29) Ethirajan, M.; Chen, Y.; Joshi, P.; Pandey, R. K. The Role of Porphyrin Chemistry in Tumor Imaging and Photodynamic Therapy. *Chem. Soc. Rev.* **2011**, *40*, 340−62.

(30) Lucky, S. S.; Soo, K. C.; Zhang, Y. Nanoparticles in Photodynamic Therapy. *Chem. Rev.* **2015**, *115*, 1990−2042.

(31) Yu, G.; Yu, S.; Saha, M. L.; Zhou, J.; Cook, T. R.; Yung, B. C.; Chen, J.; Mao, Z.; Zhang, F.; Zhou, Z. A Discrete Organoplatinum(II) Metallacage as a Multimodality Theranostic Platform for Cancer Photochemotherapy. *Nat. Commun.* **2018**, *9*, 1−18.

https://dx.doi.org/10.1021/acsnano.0c05722
ACS Nano XXXX, XXX, XXX−XXX

(32) Wigerup, C.; Påhlman, S.; Bexell, D. Therapeutic Targeting of Hypoxia and Hypoxia-Inducible Factors in Cancer. *Pharmacol. Ther.* **2016**, *164*, 152−169.
(33) Semenza, G. L. Hypoxia-Inducible Factor 1 (HIF-1) Pathway. *Science's STKE* **2007**, *2007*, No. cm8.
(34) Zhang, F. W.; Ni, Q. Q.; Jacobson, O.; Cheng, S. Y.; Liao, A.; Wang, Z. T.; He, Z. M.; Yu, G. C.; Song, J. B.; Ma, Y.; Niu, G.; Zhang, L. J.; Zhu, G. Z.; Chen, X. Y. Polymeric Nanoparticles with a Glutathione-Sensitive Heterodimeric Multifunctional Prodrug for *in Vivo* Drug Monitoring and Synergistic Cancer Therapy. *Angew. Chem., Int. Ed.* **2018**, *57*, 7066−7070.
(35) Rong, P.; Yang, K.; Srivastan, A.; Kiesewetter, D. O.; Yue, X.; Wang, F.; Nie, L.; Bhirde, A.; Wang, Z.; Liu, Z.; Niu, G.; Wang, W.; Chen, X. Photosensitizer Loaded Nano-Graphene for Multimodality Imaging Guided Tumor Photodynamic Therapy. *Theranostics* **2014**, *4*, 229−239.
(36) Ling, X.; Zhang, S.; Shao, P.; Wang, P.; Ma, X.; Bai, M. Synthesis of a Reactive Oxygen Species Responsive Heterobifunctional Thioketal Linker. *Tetrahedron Lett.* **2015**, *56*, 5242−5244.
(37) Xia, Y.; Zhang, R.; Wang, Z.; Tian, J.; Chen, X. Recent Advances in High-Performance Fluorescent and Bioluminescent RNA Imaging Probes. *Chem. Soc. Rev.* **2017**, *46*, 2824−2843.
(38) Algar, W. R.; Hildebrandt, N.; Vogel, S. S.; Medintz, I. L. FRET as A Biomolecular Research Tool-Understanding Its Potential While Avoiding Pitfalls. *Nat. Methods* **2019**, *16*, 815−829.
(39) Soh, N. Recent Advances in Fluorescent Probes for the Detection of Reactive Oxygen Species. *Anal. Bioanal. Chem.* **2006**, *386*, 532−43.
(40) Yuan, B.; Wang, H.; Xu, J.-F.; Zhang, X. Activatable Photosensitizer for Smart Photodynamic Therapy Triggered by Reactive Oxygen Species in Tumor Cells. *ACS Appl. Mater. Interfaces* **2020**, *12*, 26982−26990.
(41) Wilson, D. S.; Dalmasso, G.; Wang, L.; Sitaraman, S. V.; Merlin, D.; Murthy, N. Orally Delivered Thioketal Nanoparticles Loaded with TNF-α-siRNA Target Inflammation and Inhibit Gene Expression in the Intestines. *Nat. Mater.* **2010**, *9*, 923−928.
(42) Shim, M. S.; Xia, Y. A Reactive Oxygen Species (ROS)-Responsive Polymer for Safe, Efficient, and Targeted Gene Delivery in Cancer Cells. *Angew. Chem., Int. Ed.* **2013**, *52*, 6926−6929.
(43) Lamb, B. M.; Barbas, C. F., III Selective Arylthiolane Deprotection by Singlet Oxygen: A Promising Tool for Sensors and Prodrugs. *Chem. Commun.* **2015**, *51*, 3196−3199.
(44) Liu, L.-H.; Qiu, W.-X.; Li, B.; Zhang, C.; Sun, L.-F.; Wan, S.-S.; Rong, L.; Zhang, X.-Z. A Red Light Activatable Multifunctional Prodrug for Image-Guided Photodynamic Therapy and Cascaded Chemotherapy. *Adv. Funct. Mater.* **2016**, *26*, 6257−6269.
(45) Yin, W.; Ke, W.; Chen, W.; Xi, L.; Zhou, Q.; Mukerabigwi, J. F.; Ge, Z. Integrated Block Copolymer Prodrug Nanoparticles for Combination of Tumor Oxidative Stress Amplification and ROS-Responsive Drug Release. *Biomaterials* **2019**, *195*, 63−74.
(46) Li, S.; Xie, A.; Li, H.; Zou, X.; Zhang, Q. A Self-Assembled, ROS-Responsive Janus-Prodrug for Targeted Therapy of Inflammatory Bowel Disease. *J. Controlled Release* **2019**, *316*, 66−78.
(47) Zhu, Y.; Chen, C.; Cao, Z.; Shen, S.; Li, L.; Li, D.; Wang, J.; Yang, X. On-Demand PEGylation and DePEGylation of PLA-Based Nanocarriers *via* Amphiphilic mPEG-*TK*-Ce6 for Nanoenabled Cancer Chemotherapy. *Theranostics* **2019**, *9*, 8312−8320.
(48) Phua, S. Z. F.; Xue, C.; Lim, W. Q.; Yang, G.; Chen, H.; Zhang, Y.; Wijaya, C. F.; Luo, Z.; Zhao, Y. Light-Responsive Prodrug-Based Supramolecular Nanosystems for Site-Specific Combination Therapy of Cancer. *Chem. Mater.* **2019**, *31*, 3349−3358.
(49) Jin, H.; Zhu, T.; Huang, X.; Sun, M.; Li, H.; Zhu, X.; Liu, M.; Xie, Y.; Huang, W.; Yan, D. ROS-Responsive Nanoparticles Based on Amphiphilic Hyperbranched Polyphosphoester for Drug Delivery: Light-Triggered Size-Reducing and Enhanced Tumor Penetration. *Biomaterials* **2019**, *211*, 68−80.
(50) Oddone, N.; Pederzoli, F.; Duskey, J. T.; De Benedictis, C. A.; Grabrucker, A. M.; Forni, F.; Angela Vandelli, M.; Ruozi, B.; Tosi, G. ROS-Responsive "Smart" Polymeric Conjugate: Synthesis, Characterization and Proof-of-Concept Study. *Int. J. Pharm.* **2019**, *570*, 118655.
(51) Kim, Y.; Uthaman, S.; Pillarisetti, S.; Noh, K.; Huh, K. M.; Park, I.-K. Bioactivatable Reactive Oxygen Species-Sensitive Nanoparticulate System for Chemo-Photodynamic Therapy. *Acta Biomater.* **2020**, *108*, 273−284.
(52) Zhao, D.; Tao, W.; Li, S.; Li, L.; Sun, Y.; Li, G.; Wang, G.; Wang, Y.; Lin, B.; Luo, C.; Wang, Y.; Chen, M.; He, Z.; Sun, J. Light-Triggered Dual-Modality Drug Release of Self-Assembled Prodrug-Nanoparticles for Synergistic Photodynamic and Hypoxia-Activated Therapy. *Nanoscale Horiz.* **2020**, *5*, 886−894.
(53) Ke, W.; Li, J.; Mohammed, F.; Wang, Y.; Tou, K.; Liu, X.; Wen, P.; Kinoh, H.; Anraku, Y.; Chen, H.; Kataoka, K.; Ge, Z. Therapeutic Polymersome Nanoreactors with Tumor-Specific Activable Cascade Reactions for Cooperative Cancer Therapy. *ACS Nano* **2019**, *13*, 2357−2369.
(54) Chen, Q.; Chen, G.; Chen, J.; Shen, J.; Zhang, X.; Wang, J.; Chan, A.; Gu, Z. Bioresponsive Protein Complex of aPD1 and aCD47 Antibodies for Enhanced Immunotherapy. *Nano Lett.* **2019**, *19*, 4879−4889.
(55) Lyu, Y.; He, S.; Li, J.; Jiang, Y.; Sun, H.; Miao, Y.; Pu, K. A Photolabile Semiconducting Polymer Nanotransducer for Near-Infrared Regulation of CRISPR/Cas9 Gene Editing. *Angew. Chem., Int. Ed.* **2019**, *58*, 18197−18201.
(56) Jia, F.; Lu, X.; Tan, X.; Wang, D.; Cao, X.; Zhang, K. Effect of PEG Architecture on the Hybridization Thermodynamics and Protein Accessibility of PEGylated Oligonucleotides. *Angew. Chem., Int. Ed.* **2017**, *56*, 1239−1243.
(57) Oerlemans, C.; Bult, W.; Bos, M.; Storm, G.; Nijsen, J. F. W.; Hennink, W. E. Polymeric Micelles in Anticancer Therapy: Targeting, Imaging and Triggered Release. *Pharm. Res.* **2010**, *27*, 2569−2589.
(58) Zhou, Z.; Song, J.; Nie, L.; Chen, X. Reactive Oxygen Species Generating Systems Meeting Challenges of Photodynamic Cancer Therapy. *Chem. Soc. Rev.* **2016**, *45*, 6597−6626.
(59) Yuan, Y. Y.; Zhang, C. J.; Xu, S. D.; Liu, B. A Self-Reporting AIE Probe with a Built-in Singlet Oxygen Sensor for Targeted Photodynamic Ablation of Cancer Cells. *Chem. Sci.* **2016**, *7*, 1862−1866.
(60) Yuan, Y.; Xu, S.; Zhang, C.-J.; Zhang, R.; Liu, B. Dual-Targeted Activatable Photosensitizers with Aggregation-Induced Emission (AIE) Characteristics for Image-Guided Photodynamic Cancer Cell Ablation. *J. Mater. Chem. B* **2016**, *4*, 169−176.
(61) Gui, C.; Zhao, E. G.; Kwok, R. T. K.; Leung, A. C. S.; Lam, J. W. Y.; Jiang, M. J.; Deng, H. Q.; Cai, Y. J.; Zhang, W. J.; Su, H. F.; Tang, B. Z. AIE-Active Theranostic System: Selective Staining and Killing of Cancer Cells. *Chem. Sci.* **2017**, *8*, 1822−1830.
(62) Wang, D.; Su, H.; Kwok, R. T. K.; Hu, X.; Zou, H.; Luo, Q.; Lee, M. M. S.; Xu, W.; Lam, J. W. Y.; Tang, B. Z. Rational Design of a Water-Soluble NIR AIEgen, and Its Application in Ultrafast Wash-Free Cellular Imaging and Photodynamic Cancer Cell Ablation. *Chem. Sci.* **2018**, *9*, 3685−3693.
(63) Wang, D.; Lee, M. M. S.; Shan, G.; Kwok, R. T. K.; Lam, J. W. Y.; Su, H.; Cai, Y.; Tang, B. Z. Highly Efficient Photosensitizers with Far-Red/Near-Infrared Aggregation-Induced Emission for *in Vitro* and *in Vivo* Cancer Theranostics. *Adv. Mater.* **2018**, *30*, No. e1802105.
(64) Chavan, S. P.; Kale, R. R.; Pasupathy, K. A Facile Regioselective Decomposition of Tosylhydrazones: An Application towards the Synthesis of α-Lipoic Acid. *Synlett* **2005**, *2005*, 1129−1132.

https://dx.doi.org/10.1021/acsnano.0c05722
ACS Nano XXXX, XXX, XXX−XXX